X-ray spatial frequency heterodyne imaging of protein-based nanobubble contrast agents

Danielle Rand,[1] Masaki Uchida,[2] Trevor Douglas,[2] Christoph Rose-Petruck[1,*]

[1]*Department of Chemistry, Brown University, Providence, Rhode Island 02912, USA*
[2]*Department of Chemistry, Indiana University, Bloomington, Indiana 47405, USA*
[*]*CRosePet@Brown.edu*

Abstract: Spatial Frequency Heterodyne Imaging (SFHI) is a novel x-ray scatter imaging technique that utilizes nanoparticle contrast agents. The enhanced sensitivity of this new technique relative to traditional absorption-based x-ray radiography makes it promising for applications in biomedical and materials imaging. Although previous studies on SFHI have utilized only metal nanoparticle contrast agents, we show that nanomaterials with a much lower electron density are also suitable. We prepared protein-based "nanobubble" contrast agents that are comprised of protein cage architectures filled with gas. Results show that these nanobubbles provide contrast in SFHI comparable to that of gold nanoparticles of similar size.

OCIS codes: (340.0340) X-ray optics; (340.7440) X-ray imaging; (290.0290) Scattering; (160.4236) Nanomaterials; (160.1435) Biomaterials

References and links

1. H. Wen, E. E. Bennett, M. M. Hegedus, and S. C. Carroll, "Spatial Harmonic Imaging of X-ray Scattering - Initial Results," IEEE Trans. Med. Imaging **27**(8), 997–1002 (2008).
2. H. Wen, E. E. Bennett, M. M. Hegedus, and S. Rapacchi, "Fourier X-ray Scattering Radiography Yields Bone Structural Information," Radiology **251**(3), 910–918 (2009).
3. A. F. Stein, J. Ilavsky, R. Kopace, E. E. Bennett, and H. Wen, "Selective imaging of nano-particle contrast agents by a single-shot x-ray diffraction technique," Opt. Express **18**(12), 13271–13278 (2010).
4. B. Wu, Y. Liu, C. Rose-Petruck, and G. J. Diebold, "X-ray spatial frequency heterodyne imaging," Appl. Phys. Lett. **100**(6), 061110 (2012).
5. Y. Liu, B. Ahr, A. Linkin, G. J. Diebold, and C. Rose-Petruck, "X-ray spatial harmonic imaging of phase objects," Opt. Lett. **36**(12), 2209–2211 (2011).
6. D. Rand, V. Ortiz, Y. Liu, Z. Derdak, J. R. Wands, M. Tatíček, and C. Rose-Petruck, "Nanomaterials for X-ray Imaging: Gold Nanoparticle Enhancement of X-ray Scatter Imaging of Hepatocellular Carcinoma," Nano Lett. **11**(7), 2678–2683 (2011).
7. M. Uchida, S. Kang, C. Reichhardt, K. Harlen, and T. Douglas, "The ferritin superfamily: Supramolecular templates for materials synthesis," Biochim. Biophys. Acta **1800**(8), 834–845 (2010).
8. J. Lucon, S. Qazi, M. Uchida, G. J. Bedwell, B. LaFrance, P. E. Prevelige, Jr., and T. Douglas, "Use of the interior cavity of the P22 capsid for site-specific initiation of atom-transfer radical polymerization with high-density cargo loading," Nat. Chem. **4**(10), 781–788 (2012).
9. D. P. Patterson, P. E. Prevelige, and T. Douglas, "Nanoreactors by Programmed Enzyme Encapsulation Inside the Capsid of the Bacteriophage P22," ACS Nano **6**(6), 5000–5009 (2012).
10. D. P. Patterson, B. Schwarz, K. El-Boubbou, J. van der Oost, P. E. Prevelige, and T. Douglas, "Virus-like particle nanoreactors: programmed encapsulation of the termostable CelB glycosidase inside the P22 capsid," Soft Matter **8**(39), 10158–10166 (2012).
11. D. P. Patterson, A. Rynda-Apple, A. L. Harmsen, A. G. Harmsen, and T. Douglas, "Biomimetic Antigenic Nanoparticles Elicit Controlled Protective Immune Response to Influenza," ACS Nano **7**(4), 3036–3044 (2013).
12. T. Douglas and M. Young, "Host–guest encapsulation of materials by assembled virus protein cages," Nature **393**(6681), 152–155 (1998).
13. S. Kang and T. Douglas, "Biochemistry. Some Enzymes Just Need a Space of Their Own," Science **327**(5961), 42–43 (2010).
14. B. Wörsdörfer, K. J. Woycechowsky, and D. Hilvert, "Directed Evolution of a Protein Container," Science **331**(6017), 589–592 (2011).
15. M. L. Flenniken, L. O. Liepold, B. E. Crowley, D. A. Willits, M. J. Young, and T. Douglas, "Selective attachment and release of a chemotherapeutic agent from the interior of a protein cage architecture," Chem. Commun. (Camb.) **28**(4), 447–449 (2005).

16. Y. P. Ren, S. M. Wong, and L. Y. Lim, "Application of Plant Viruses as Nano Drug Delivery Systems," Pharm. Res. **27**(11), 2509–2513 (2010).
17. L. O. Liepold, M. J. Abedin, E. D. Buckhouse, J. A. Frank, M. J. Young, and T. Douglas, "Supramolecular Protein Cage Composite MR Contrast Agents with Extremely Efficient Relaxivity Properties," Nano Lett. **9**(12), 4520–4526 (2009).
18. K. Li, H. G. Nguyen, X. B. Lu, and Q. Wang, "Viruses and Their Potential in Bioimaging and Biosensing Applications," Analyst (Lond.) **135**(1), 21–27 (2009).
19. P. D. Garimella, A. Datta, D. W. Romanini, K. N. Raymond, and M. B. Francis, "Multivalent, High-Relaxivity MRI Contrast Agents Using Rigid Cysteine-Reactive Gadolinium Complexes," J. Am. Chem. Soc. **133**(37), 14704–14709 (2011).
20. M. L. Flenniken, D. A. Willits, A. L. Harmsen, L. O. Liepold, A. G. Harmsen, M. J. Young, and T. Douglas, "Melanoma and lymphocyte cell-specific targeting incorporated into a heat shock protein cage architecture," Chem. Biol. **13**(2), 161–170 (2006).
21. N. Stephanopoulos, G. J. Tong, S. C. Hsiao, and M. B. Francis, "Dual-Surface Modified Virus Capsids for Targeted Delivery of Photodynamic Agents to Cancer Cells," ACS Nano **4**(10), 6014–6020 (2010).
22. T. Douglas and M. Young, "Viruses: Making Friends with Old Foes," Science **312**(5775), 873–875 (2006).
23. L. A. Lee and Q. Wang, "Adaptations of Nanoscale Viruses and Other Protein Cages for Medical Applications," Nanomedicine **2**(3), 137–149 (2006).
24. M. Uchida, M. T. Klem, M. Allen, P. Suci, M. Flenniken, F. Gillitzer, Z. Varpness, L. O. Liepold, M. Young, and T. Douglas, "Biological Containers: Protein Cages as Multifunctional Nanoplatforms," Adv. Mater. **19**(8), 1025–1042 (2007).
25. A. de la Escosura, R. J. M. Nolte, and J. J. L. M. Cornelissen, "Viruses and Protein Cages as Nanocontainers and Nanoreactors," J. Mater. Chem. **19**(16), 2274–2278 (2009).
26. L. Shen, N. Bao, Z. Zhou, P. E. Prevelige, and A. Gupta, "Materials Desing Using Genetically Engineered Proteins," J. Mater. Chem. **21**(47), 18868–18876 (2011).
27. I. Yildiz, S. Shukla, and N. F. Steinmetz, "Applications of Viral Nanoparticles in Medicine," Curr. Opin. Biotechnol. **22**(6), 901–908 (2011).
28. L. A. Lee, Z. W. Niu, and Q. Wang, "Viruses and Virus-like Protein Assemblies - Chemically Programmable Nanoscale Building Blocks," Nano Res. **2**(5), 349–364 (2009).
29. M. Uchida, M. L. Flenniken, M. Allen, D. A. Willits, B. E. Crowley, S. Brumfield, A. F. Willis, L. Jackiw, M. Jutila, M. J. Young, and T. Douglas, "Targeting of Cancer Cells with Ferrimagnetic Ferritin Cage Nanoparticles," J. Am. Chem. Soc. **128**(51), 16626–16633 (2006).
30. M. L. Galisteo and J. King, "Conformational Transformations in the Protein Lattice of Phage P22 Procapsids," Biophys. J. **65**(1), 227–235 (1993).
31. J. V. Jokerst, T. Lobovkina, R. N. Zare, and S. S. Gambhir, "Nanoparticle PEGylation for imaging and therapy," Nanomedicine **6**(4), 715–728 (2011).
32. E. Sadauskas, H. Wallin, M. Stoltenberg, U. Vogel, P. Doering, A. Larsen, and G. Danscher, "Kuppfer cells are central in the removal of nanoparticles from the organism," Part. Fibre Toxicol. **4**(10), 1–7 (2007).
33. E. Sadauskas, G. Danscher, M. Stoltenberg, U. Vogel, A. Larsen, and H. Wallin, "Protracted elimination of gold nanoparticles from mouse liver," Nanomedicine **5**(2), 162–169 (2009).

1. Introduction

Spatial Frequency Heterodyne Imaging (SFHI) is a novel x-ray imaging technique developed in recent years that uses x-rays scattered by a sample to form an image [1–4]. SFHI is based on a linear arrangement of x-ray source, tissue, and x-ray detector, much like that of a conventional x-ray imaging apparatus. However, SFHI rests on a complete paradigm reversal compared to conventional x-ray absorption-based radiology, in which scattered x-rays are rejected to enhance the image contrast. Benefits of SFHI compared to absorption-based x-ray imaging include its improved sensitivity and its ability to yield anisotropic information regarding how the object being imaged scatters incident x-rays [5, 6].

The use of gold and iron oxide nanoparticle contrast agents has been proven to further enhance the sensitivity of SFHI [3, 6]. Specifically, AuNPs have been utilized as SFHI contrast agents for the imaging of human Hepatocellular Carcinoma, with results demonstrating that SFHI is capable of distinguishing between cancer tissue labeled with AuNPs and tissue that is unlabeled [6]. Until recently, this application of SFHI for biomedical imaging was centered on the idea that the increased electron density of the metal nanoparticle contrast agents (relative to typical biological tissues) was required to improve the visibility of nanoparticle-targeted tissues in SFHI x-ray scatter images.

However, we have recently discovered that high electron density materials are not necessary for providing contrast in SFHI. Rather, the only requirement for a x-ray scatter

contrast agent to be used in biomedical imaging applications is an electron density that differs from that of the biological tissues being studied. As such, a wide variety of different types of nanoparticles including those with very low electron density should be suitable. To this end, we present the development of a novel protein-based nanoparticle contrast agent comprised of nano-sized protein cage architectures that are filled with perfluoropropane (C_3F_8) gas. The protein assemblies used to make these "nanobubble" contrast agents are apoferritin (approximately 12 nm outer diameter) [7] and a virus-like particle (VLP) derived from the Salmonella typhimurium bacteriophage P22 capsid (approximately 60 nm outer diameter) [8–11].

Protein cage structures such as those mentioned above have been studied for their potential in materials synthesis [7, 12], catalysis [13, 14], drug and gene delivery [15, 16], bio-imaging [17–19], cell targeting [20, 21], and vaccine development [11]. VLPs in particular are promising, as they exist in a large range of sizes (tens to hundreds of nanometers), have well-defined, monodisperse structures, can be purified in large quantities, and can be easily modified both genetically and chemically [22–27]. Their flexibility has facilitated the design of bionanomaterials with multiple functionalities via modification of the inner and outer capsid surfaces. For example, previous studies have shown that VLPs can both encapsulate various cargoes (including small molecules, polymers, enzymes, nanoparticles, and nucleic acids) and be surface-modified with antibodies, peptides, and other ligands [28]. It should therefore be possible to combine the imaging capabilities of the nanobubble contrast agents proposed here with targeting and therapeutic functionalities.

Contrast agents based on protein cage architectures have previously been developed and applied for bio-imaging. Examples include VLPs encapsulating fluorophores for fluorescence imaging and VLPs encapsulating gadolinium or iron oxide compounds for magnetic resonance imaging (MRI) [7, 17–19]. However, this study represents the first time such structures have been applied as contrast agents in x-ray imaging.

The nanobubble formulation proposed here is similar to that used for the design of contrast agents in ultrasound imaging. For example, Optison is an ultrasound contrast agent consisting of an aqueous suspension of 4 μm diameter albumin shells filled with perfluoropropane gas (C_3F_8) [26]. Optison has been proven to work well as a contrast agent for SFHI [5]; however, the size of the protein shells limits their possible *in vivo* applications. Nano-sized protein-based contrast agents such as those described here would be much more versatile and could be used for the *in vivo* targeting and imaging of individual cells.

2. Materials and methods

2.1. Gold nanoparticles

Gold nanoparticles (AuNPs) of 10 nm and 50 nm diameter in citrate buffer were purchased from British Biocell International (Cardiff, UK). Prior to x-ray imaging, AuNPs were stabilized with a coating of thiol-functionalized polyethylene glycol (PEG). HS-PEG-COOH (M_w = 3000) was purchased from Sigma Aldrich (St. Louis, MO) and prepared at 100 μM in ultrapure water. To 50 μg of as-purchased AuNPs in water, 140 μl of PEG (for 10 nm AuNPs) or 28 μl of PEG (for 50 nm AuNPs) was added and stirred overnight at room temperature. The chains of functionalized PEG attach to the surface of the AuNPs during this mixing, replacing the citrate stabilizer due to the affinity of thiols for gold. Excess PEG was removed by centrifugation, and the resulting PEG-coated AuNPs were resuspended in ultrapure water.

2.2 Protein-based nanoparticles

Human heavy-chain ferritin (HFn) and the procapsid (PC) form of P22 were heterologously expressed in *E. coli* BL21 (DE3) and purified as previously described [8, 29]. P22 scaffolding protein was extracted to prepare the empty shell (ES) form of P22 VLP using a buffer (50mM

sodium phosphate and 100 mM sodium chloride at pH 7.0) containing 0.5M of guanidine-HCl followed by ultracentrifugation of the capsid [8] to pellet the capsid, which was subsequently resuspended in the same buffer. This extraction process was repeated four times. The expanded shell (Ex) form of the P22 VLP was prepared by heating the P22 procapsid at 65°C for 20 min [30].

Just prior to lyophilization, ferritin and P22 VLP (both ES and Ex forms) were dialyzed against water and a buffer (2 mM sodium phosphate and 30 mM sodium chloride at pH 7.4), respectively. One ml of each protein (2mg/ml) was aliquoted into a glass vial, quickly frozen in a liquid nitrogen bath, and then lyophilized. The glass vials were sealed with a septum cap, and subject to evacuation and back-filling with C_3F_8 gas (at 1atm) twice. While under C_3F_8 gas atmosphere, 0.4 ml of water was added to each vial via a syringe through the septum to reconstitute the lyophilized protein with gas trapped inside the protein cage.

2.3 Preparation of samples for X-ray imaging

For x-ray imaging, all samples were prepared in ultrapure water at concentrations of 1 mg scattering material/ml: AuNP samples (2 total) contained 1 mg Au/ml and protein nanobubble samples (9 total) contained 1 mg protein/ml. Samples were placed in a glass tube and held in an aluminum holder alongside a control sample (a glass tube containing ultrapure water alone). Three x-ray absorbance and three x-ray scatter images were taken of each sample. Signals measured for the 11 samples were normalized relative to that measured for the water control. Results given in the text are the average and standard deviation of normalized signals measured over each set of three images.

2.4 Spatial Frequency Heterodyne Imaging

The x-ray imaging technique applied here, called Spatial Frequency Heterodyne Imaging [1–6], uses x-rays scattered by the sample to form an image. The object being imaged deflects incident x-rays from the primary beam direction, and this deflection can be detected by placing a grid between the sample and the x-ray source (see Fig. 1).Without sample, the image of the grid is sharp and is limited only by the resolution of the imaging system. Introduction of the sample, however, yields scattered x-rays that cause a blurring of the grid image. The extent of this blurring corresponds to the amount of x-rays that are scattered by the sample, and is therefore a measure of nanoparticle concentration when such contrast agents are utilized. The imaging theory is discussed elsewhere [4].
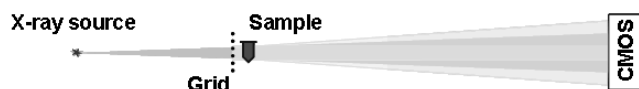

Fig. 1. Schematic of the x-ray imaging setup.

Acquired images can be analyzed by a procedure involving Fourier transformation. The intensity modulations in an image taken of sample with a grid are proportional to the product of the x-ray transmittances of the sample and of the grid. Thus, Fourier transformation of the image converts this product into a convolution in the spatial frequency domain. The grid, a periodic structure, produces a series of peaks in this convolution, and each peak is surrounded by the spatial frequency spectrum of the sample. The areas surrounding all peaks in the convolution therefore contain the same information regarding x-ray transmittance through the sample. X-ray scatter does not influence the intensities around the central, zero-frequency peak, but does influences the intensities around all other higher order peaks. Selecting an area around the zero-order peak and an area around at least one other higher order peak and Fourier back-transforming these areas results in two separate images. The image h_0 from the

zero-order area contains only x-ray transmittance information. The image h_x from the higher order area contains both x-ray transmittance and x-ray scatter information. For normalization purposes, an image is acquired without sample and processed following the same Fourier procedure, resulting in one zero-order image g_0 and one higher-order image g_x of the grid. Subsequently, a normalized absorbance image and one or more normalized scatter images are produced according to Eq. (1) and Eq. (2).

$$A = -\log_{10}\left(\frac{h_0}{g_0}\right)$$ (1)

$$S = -\log\left(\frac{h_x / g_x}{h_0 / g_0}\right)$$ (2)

Thus, S consists exclusively of scattered x-rays because the transmittance component is normalized out. By convention, the absorbance A is defined as the logarithm of the ratio of the transmittances h_0 and h_x. The scattered intensity S is the logarithm of the amount of scattered radiation.

The numerical process by which x-ray absorbance and x-ray scatter images are produced in SFHI is depicted in Fig. 2. The zero-order peak (blue box) in the convolution yields the absorbance image A. The 1st order peaks (red and yellow boxes) in the convolution yield the scatter images S. Note that the left 1st order peak (red box) contains radiation scattered only in the horizontal direction; by convention we label this image the "1,0" scatter image after processing. Similarly, the upper 1st order peak (yellow box) corresponds to scattering in the vertical direction, and gives a "0,1" scatter image after processing. Thus, every x-ray image taken yields three types of processed images; one corresponding to x-radiation absorbed by the sample, one corresponding to x-radiation scattered horizontally by the sample, and one corresponding to x-radiation scattered vertically by the sample. It should be noted that although this technique is capable of giving anisotropic scattering information, both 1st order x-ray images should measure identical scatter signals when isotropically-oriented nanoparticles (such as the nanobubbles employed here) are used as SFHI contrast agents. The only difference between the horizontal and vertical x-ray scatter images that can be seen is the enhancement of the side interfaces of the glass tubes with air in the horizontal x-ray scatter image (see Fig. 2). This effect is due to the anisotropic x-ray scattering at smooth material interfaces.

The measurements were done with a microfocus X-ray tube (Trufocus Corp., model TFX-3110EW) with a tungsten anode. The tube was operated at an electrical power of 16W, with a maximum voltage of 80 kV. High voltages are used to reduce required exposure times; they are also better suited for applications requiring large penetration depths. The distance between the source and sample is 0.4 m, and the distance between the sample and detector is 1.2 m. The grid used is a nickel wire mesh with a pitch of approximately 170 μm and a wire thickness of 66 μm. The grid was purchased from Small Parts, Inc. (Seattle, WA), and was positioned between the x-ray source and the sample, directly in front of the sample. The images were acquired with an x-ray CMOS detector (Rad-Icon Imaging, RadEye200 model). The total exposure time for each image was 180 s. X-ray transmission through the grid for this exposure time at the x-ray tube settings described above is approximately 80%.
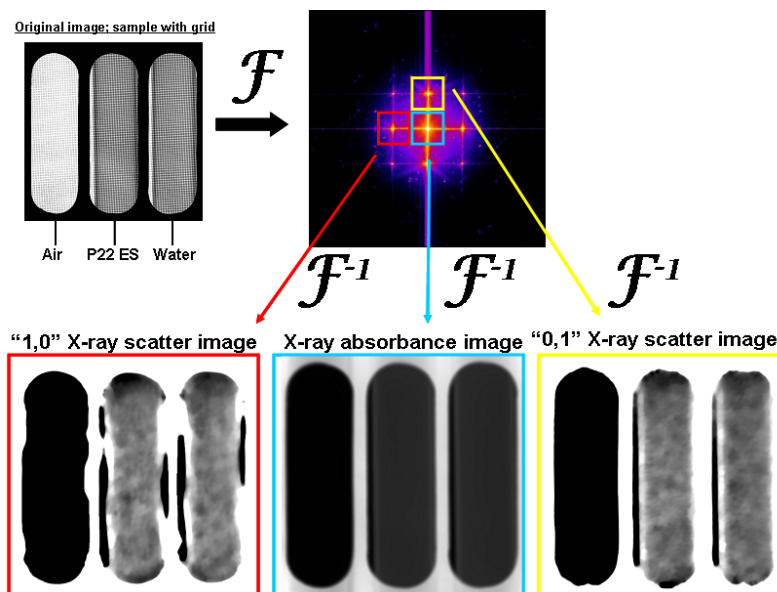
Fig. 2. X-ray scatter images are produced via numerical processing of an absorption-based x-ray image. An image with grid and sample placed in the x-ray beam path (top left) gives a convolution in the spatial frequency domain (top right) after Fourier transformation. Different peaks in the spatial frequency spectrum (surrounded by colored boxes) contain different information regarding how the sample scatters and absorbs incident x-radiation. The samples shown in the original image are glass tubes containing the P22 ES nanobubble suspension (middle) and water (right).

3. Results

The three "nanobubble" contrast agents studied here were prepared from three different protein cage architectures. The smallest nanobubble was prepared using apoferritin, a protein cage with an outer diameter of approximately 12 nm and inner diameter of approximately 8 nm [7, 23]. The larger nanobubbles were prepared using two distinct morphologies of a virus-like particle (VLP) derived from the Salmonella typhimurium bacteriophage P22 capsid. This VLP is a protein cage composed of 420 subunits of a 46.6 kDa coat protein that assemble into an icosahedral capsid with the aid of a scaffolding protein [8–11]. The first VLP morphology used here is the empty shell formulation of the VLP (P22 ES), in which the scaffolding protein has been removed; the resulting protein cage has an outer diameter of approximately 58 nm and an inner diameter of approximately 48 nm. The second VLP morphology used is the expanded shell formulation of the VLP (P22 EX), which is formed when gentle heating causes the VLP to expand to a protein cage with an outer diameter of approximately 64 nm and inner diameter of approximately 54 nm. To prepare the contrast agent, all three protein cage architectures were lyophilized, filled with perfluoropropane gas (C_3F_8) and resuspended in water. The hydrophobic gas remains trapped within the protein cages for at least several days and perhaps much longer. Further studies are needed to determine the long-term stability of the contrast agents.

To analyze their ability to scatter x-rays, the three contrast agents were suspended in water at a concentration of 1 mg protein/ml and imaged by SFHI. A sample containing water alone was used as reference. Analysis of the images involved measuring the signals detected for the nanobubble samples and normalizing them relative to the signal detected for the sample containing only water. To compare the nanobubbles to contrast agents used previously in SFHI, samples containing gold nanoparticles of comparable size were also prepared at 1 mg Au/ml and imaged by SFHI. The contrast provided by the larger P22 nanobubbles was compared to that of 50 nm AuNPs, while the contrast provided by the smaller ferritin

nanobubbles was compared to that of 10 nm AuNPs. The subsequent signal enhancements over water for both the nanobubbles and the AuNPs as measured from SFHI x-ray scatter images are reported as percentages in Table 1. The results indicate that when nanobubbles and AuNPs of similar sizes are prepared at equal concentrations by mass, they provide comparable contrast in SFHI, showing 6-8% x-ray scatter signal enhancement over water alone. The P22 EX nanobubbles are stronger x-ray scatterers than the P22 ES and ferritin nanobubbles by a small but statistically significant amount. This effect is likely due to the larger diameter of the P22 EX particles.

Table 1. X-Ray Scatter Signal Enhancements of Nanoparticle Contrast Agents

Sample	X-ray Scatter Signal Enhancement (%)
50 nm AuNP	8.2 ± 0.4
10 nm AuNP	6.5 ± 0.4
P22 ES	7.1 ± 0.2
Sonicated P22 ES	1.0 ± 0.1
P22 ES shell	1.2 ± 0.2
P22 Ex	7.5 ± 0.1
Sonicated P22 Ex	$1.6 \pm >0.1$
P22 Ex shell	0.2 ± 0.1
Ferritin	6.7 ± 0.2
Sonicated Ferritin	$0.0 \pm >0.1$
Ferritin shell	1.8 ± 0.2

To prove that the contrast provided by the nanobubbles is due to the reduced electron density (relative to water) of the encapsulated gas, and not the scattering ability of the protein shell itself, the nanobubble samples discussed above were sonicated for 1h. Sonication should rupture the nanobubbles while leaving the elemental composition of the sample intact. Sonication causes the signal enhancement of the sample to drop 88% on average, from approximately 7% to less than 1% (see Table 1). Additionally, samples containing protein cages that had not been filled with gas (but retained their approximate size and shape) were suspended in water at 1 mg/ml and imaged by SFHI. The results show that these gasless samples also did not provide appreciable contrast in the resulting x-ray scatter images, showing an 84% drop on average relative to the gas-filled nanobubbles (see Table 1). The data therefore suggest that only when the protein cages are intact and have encapsulated gas do they scatter x-rays in quantities comparable to that of gold nanoparticles of a similar size (see Fig. 3).
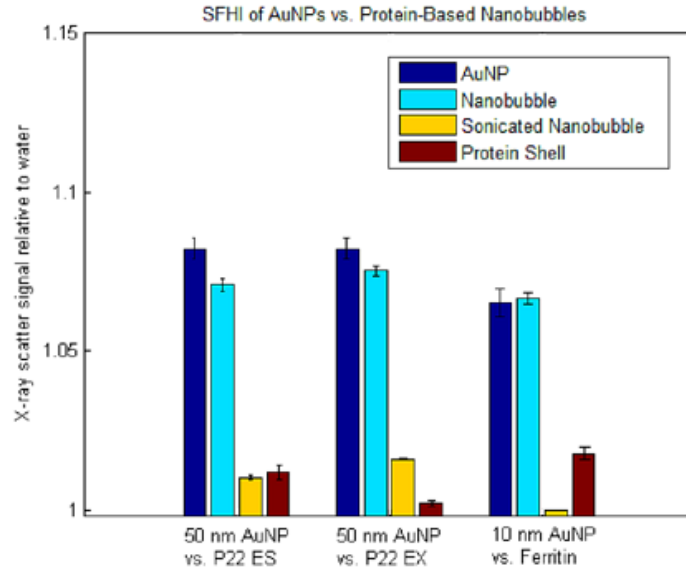
Fig. 3. SFHI x-ray scatter signal enhancements over water for protein cage architectures and gold nanoparticles of comparable size. Protein cages were imaged intact and filled with perfluoropropane gas (nanobubble formulation, light blue bars); after sonication (yellow bars) and intact but devoid of gas (red bars). Error bars represent one standard deviation of the mean. The error bar for the x-ray scatter signal of the sonicated Ferritin nanobubble suspension is too small to be seen relative to the size of the x-ray scatter signals of the AuNPs and inflated nanobubbles.

It is also important to note that SFHI is much more sensitive to the contrast provided by the nanobubble contrast agents than conventional x-ray imaging. Absorption-based x-ray images were also taken of the three nanobubble contrast agents, and their signal enhancements relative to water are given as percentages in Table 2. When x-ray absorbance images are compared to x-ray scatter images, we find that the x-ray scatter signal enhancements over water are greater than X-ray absorbance signal enhancements by an average factor of approximately 60.

Table 2. Comparison of X-ray Absorbance and Scatter Signal Enhancements

Sample	X-ray Absorbance Signal Enhancement (%)	X-ray Scatter Signal Enhancement (%)
P22 ES	$0.14 \pm {<}0.01$	7.1 ± 0.2
P22 Ex	$0.09 \pm {<}0.01$	7.5 ± 0.1
Ferritin	$0.15 \pm {<}0.01$	6.6 ± 0.2

4. Discussion

4.1 Nanobubble preparation and imaging

The nanobubble x-ray contrast agents prepared here are the first of their kind. Results indicate that the contrast provided by this novel bionanomaterial in SFHI is comparable to that provided by AuNPs. We can therefore reasonably expect that results obtained in the past using AuNP contrast agents in SFHI (for example, the differentiation of nanoparticle-labeled and unlabeled liver cancer tissue) [6] should be possible with nanobubbles as well. As such, the proposed nanobubbles contrast agents could have applications in diagnostic imaging and monitoring cancer growth.

It should also be possible to combine the biomedical imaging function of the nanobubbles with other properties due to the flexibility of VLPs, as it is possible to modify both the inner

and outer surfaces of these capsids. For example, VLPs have been targeted to specific cells including melanoma cells and lymphocytes by attaching antibodies and peptides to their outer surface [20]. They have also been used for the delivery of chemotherapeutic agents such as the anticancer drug doxorubicin [15] and photodynamic agents like singlet oxygen [21], both of which were encapsulated inside the protein cage.

Toxicity and immune response are issues that need to be addressed before clinical application. However, these issues could be dealt with in part by modifying the outer surfaces of VLPs with polyethylene glycol (PEG), which has been shown to reduce bioactivity and increase the circulation time of nanoparticles in the bloodstream [31]. Furthermore, VLPs are biocompatible and biodegradable, and they are considered non-infections and non-hazardous in humans [27]. The fact that VLPs can be broken down in the body is important for their clinical application as contrast agents; this is especially true relative to AuNPs, which are nontoxic but can only be cleared from the body when they are smaller than approximately 5 nm in diameter [32, 33]. VLPs can also be purified in large quantities relatively inexpensively, which could make them cost-effective alternatives to the metal nanoparticle contrast agents used for SFHI in the past [23, 24].

One important fact to note is that the nanobubbles and gold nanoparticles scatter x-rays in comparable amounts when prepared at the same concentration by mass (in this study, 1 mg scattering material/ml H_2O). As gold nanoparticles are much denser than their nanobubble counterparts, however, an equal mass of gold and protein translates to a large discrepancy in the number of particles in the solution (see Table 3). We can therefore conclude that each individual AuNP scatters x-rays 10 to 20 times stronger than each individual protein-based nanobubble.

Table 3. Particle Number Densities in Contrast Agent Samples

Sample (1 mg/ml)	Concentration by number (particles/ml)
50 nm AuNP	7.9×10^{11}
10 nm AuNP	9.9×10^{13}
P22 ES nanobubble	3.1×10^{13}
P22 Ex nanobubble	3.1×10^{13}
Ferritin nanobubble	1.3×10^{15}

By mass, however, the nanobubbles prepared here appear to be just as effective as AuNPs when used as contrast agents in SFHI. Furthermore, we have shown that this scattering power derives not from the protein cage itself, but from the filling of the protein cage with gas. Our study has therefore proven that materials with both high and low electron density are capable of providing contrast in x-ray scatter imaging. This discovery improves the versatility of the novel x-ray imaging technique, as is it not specific any particular material for contrast, and when applied in vivo could utilize protein-based nanoparticles that may be more biocompatible than the metal nanoparticles used in the past. Furthermore, the enhanced sensitivity of SFHI relative to conventional absorption-based x-ray imaging is especially pronounced when VLPs are used as contrast agents; x-ray scatter signal enhancements over water are more than an order of magnitude greater than x-ray absorbance signal enhancements. Further tests and development of the nanobubble contrast agents (with modification of the inner and outer surfaces of the protein cages) could enable targeted diagnostic imaging and therapy.

Acknowledgements